Spectral variability of the binary HR 4049 * **

Eric J. Bakker[1], **David L. Lambert**[1], **Hans van Winckel**[2], **James K. McCarthy**[1,3], **Christoffel Waelkens**[2], **and Guillermo Gonzalez**[1,4]

[1] Department of Astronomy and W.J. McDonald Observatory, University of Texas, Austin, TX 78712-1083, USA, ebakker@astro.as.utexas.edu, dll@astro.as.utexas.edu

[2] Astronomical Institute, Catholic University of Leuven, Celestynenlaan 200, B-3030 Heverlee, Belgium, Hans.VanWinckel@wis.kuleuven.ac.be, christoffel@ster.kuleuven.ac.be

[3] Department of Astronomy MS 105-24, Caltech, Pasadena, CA 91125, USA, jkm@optkos.caltech.edu

[4] Department of Astronomy, University of Washington, P.O. Box 351580, Seattle, WA 98195-1580, USA, gonzalez@orca.astro.washington.edu

arXiv:astro-ph/9802120v1 10 Feb 1998

Abstract. The C I, Na I D, and Hα lines of the post-AGB binary HR 4049 have been studied. Na I D variability results from a photospheric absorption component ([Na/H]=-1.6 ± 0.2) which follows the velocity of the primary and a stationary, non-photospheric component. An emission component is attributed to the circumbinary disc, and an absorption component to mass-loss from the system with a velocity of 5.3 ± 0.5 km s^{-1}.

The Hα profile varies with the orbital period. The two strong shell type emission peaks are identified as from one single broad emission feature with an absorption centered around -7.5 km s^{-1}. The intensity variations are largely attributed to a differential amount of reddening towards the Hα emitting region and the stellar continuum. The radial velocities suggest that the Hα emission moves in phase with the primary, but with a slightly lower velocity amplitude. From this we infer that the Hα emission comes from outside the orbit of the primary, but still gravitational bound to the primary. Hα also shows a weak emission feature at -21.3 ± 3.5 km s^{-1}, which originates from the circumbinary disc and a weak absorption feature at -7.5 ± 1.6 km s^{-1} due to absorption by the circumbinary disc.

We propose two competing models that could account for the observed velocity and intensity variations of the Hα profile. Model I: light from the primary reflects on a localized spot near the inner radius of the circumbinary disc which is closest to the primary. Model II: Hα emission originates in the outer layers of the extended atmosphere of the primary due to activity. These activities are locked to the position of the primary in its orbit.

We discuss the similarities of variability and shape of the Hα emission of HR 4049 with those of early type T-Tauri stars (e.g SU Aur).

Key words: line formation – line profiles – AGB and post-AGB stars – close binaries – emission line stars – individual stars: HR 4049

---

1. Introduction

With [Fe/H] ≈ -4.8, HR 4049 is the prototype of a group of high-latitude supergiant binary stars with an extremely metal-depleted photosphere (van Winckel et al. 1995 and references therein). Their high luminosity, position above the Galactic plane and in most cases observationally confirmed C-rich circumstellar dust, suggest that they are in a post-AGB phase of evolution. The observed photospheric abundance patterns (low abundances of chemical elements with high dust condensation temperature and high abundance of elements with low dust condensation temperature) can best be explained by a model in which circumstellar gas, devoid of refractory elements, is accreted on the star, coating it with a chemically peculiar layer (Venn & Lambert 1990; van Winckel et al. 1992). For the extremely metal-depleted post-AGB stars, the gas-dust separation occurs in a circumbinary disk (Waters et al. 1992) but the question of the efficiency of the process gained momentum after the findings of Giridhar et al. (1994), Gonzalez et al. (1997a and 1997b), and Gonzalez & Wallerstein (1996) that also the photosphere of Galactic RV Tauri stars and

the binary type II Cepheid ST Pup show the same depletion pattern.

HR 4049 is a binary system with an orbital period of 430 days (Waelkens et al. 1991a). All other members of the group of metal-depleted post-AGB binaries have orbital periods of the order of one to several years (van Winckel et al. 1995). With an estimated stellar radius of 47 $R_\odot$, the primary of HR 4049 fits nicely within the binary system. However, single star evolution predicts a stellar radius of about 250 $R_\odot$ at the tip of the AGB (Boothroyd & Sackmann 1988). Since the minimum separation between the two stars is 190 $R_\odot$ this would lead to a phase of common envelope evolution (case C Roche lobe overflow). Evidently, the system survived this phase, or did not experience it. Either way, we expect that the stellar masses of the two bodies might have been altered.

HR 4049 shows photometric variations which are attributed to a phase-dependent circumsystem reddening (Waelkens et al. 1991a) from a circumbinary disc (CBD). The inclination of the system is not known, but both edge-on and face-on are excluded since the circumsystem reddening is phase-dependent. Supporting evidence for a CBD comes from the presence of large dust grains ($> 0.8\ \mu m$) as inferred from the polarimetric measurements by Joshi et al. (1987), and the presence of relatively hot dust close to the star (Lamers et al. 1986).

In order to understand the environment of HR 4049, we have made a detailed study of the variability of the C I, Na I D and Hα lines of HR 4049. In Sect. 2 we present the observations and in Sect. 3 re-derive the orbital parameters. The variability of the Na D lines is described in Sect. 4 and of Hα in Sect. 5. In Sect. 6 we propose two competing models to account for the Hα variability. A discussion is presented in Sect. 7.

2. Observations and data reduction

High-resolution (typically $R = \lambda/\Delta\lambda > 50,000$), high signal-to-noise spectra of HR 4049 were obtained over the past decade. Six different instruments were used on five different telescopes at four locations worldwide. In total sixty Hα and thirty-two Na I D spectra are available that sample the orbital phase. Tables 3 and 4 list for each available spectrum the civil (mm/dd/yyyy) and heliocentric Julian date (HJD), the absolute phase (taking $\phi_{\mathrm{abs}} = 0.0$ at $HJD = T_0$, see Table 1 for details), the telescope/instrument, spectral resolving power, the stellar heliocentric radial velocity and average error as determined from the given photospheric lines. The observations will be discussed starting with the largest subsample and continuing in order of decreasing size of the subsample.

CAT/CES: Twenty-three Hα and two Na I D single-order spectra ($R \sim 55,000$) have been obtained by HvW and CW on the ESO observatory at La Silla (Chili) using the coudé echelle spectrograph at the 1.4m Coudé Auxiliary Telescope.

McD/CS11: Twenty-three Hα and twenty-one Na I D single-order spectra ($R \sim 60,000$) have been obtained by DLL, JKM, and Jos Tomkin using the echelle spectrograph (6-foot camera) on the 2.7m McDonald telescope.

McD/CE: Ten multi-order spectra ($R \sim 45,000$) have been obtained by GG using the Sandiford cassegrain echelle spectrograph (McCarthy et al. 1993) on the 2.1m McDonald telescope. Eight contain Hα and four Na I D.

WHT/UES: Three multi-order spectra ($R \sim 50,000$) have been obtained in service time using the Utrecht echelle spectrograph on the 4.2m William Herschel telescope on La Palma (Unger 1994). All three spectra contain the Hα, Na I D, and numerous photospheric absorption lines. An extensive analysis of these spectra and a complete line identification have been published in Paper I (Bakker et al. 1996).

McD/CS21: Two multi-order spectra ($R \sim 160,000$) have been obtained by EJB using the cross-dispersed echelle spectrograph (Tull et al. 1995) at the 2.7m McDonald telescope. Both contain Hα and Na I D.

CTIO/ES: One single-order Hα spectrum ($R \sim 18,000$) has been obtained by Andy McWilliam using the echelle spectrograph with the air Schmidt camera on the 4m CTIO telescope.

Spectra have been reduced by a number of people, each using their preferred data reduction software (MIDAS, IRAF, or FIGARO). All spectra were bias subtracted, flat fielded, wavelength calibrated, and continuum corrected.

3. Stellar, orbital, and photometric parameters for HR 4049

3.1. Stellar parameters

Lambert et al. (1988) and Waelkens et al. (1991b) have determined the stellar parameters of HR 4049: $T_{\mathrm{eff}} \simeq 7500$ K and $\log g \simeq 1.0$. The chemical abundance of the photosphere is not a good indicator for the dredge-up history of the star since the photospheric abundance pattern has been modified by the gas-dust separation process (van Winckel et al. 1992, Mathis & Lamers 1992). The infrared spectrum of HR 4049 reveals emission lines (PAHs) which are attributed to carbon-rich material, while silicate emission lines are absent (Buss et al. 1990, Molster et al. 1996). This suggests that HR 4049 has passed the third dredge-up phase on the AGB. We assume that HR 4049 has the luminosity and radius of a normal, single, post-AGB star that is evolving to the White Dwarf (WD) cooling track. The distribution of masses of hydrogen-rich DA WDs is strongly peaked around 0.56 $M_\odot$ (Bergeron et al. 1992). In the absence of a direct measurement of the mass of HR 4049 we will take this WD mass to be the mass of the primary of HR 4049. From the effective gravity and core mass we find $R_A = 40\ R_\odot$ and $\log L_A/L_\odot = 3.7$ (the subscript A refers to the observed component, and B to the unseen component of the binary system). An alternative

path to the radius and luminosity is by means of the core-mass luminosity relation (Boothroyd & Sackmann 1988): $\log L_A/L_\odot = 3.8$ and hence $R_A = 47$ $R_\odot$. We will adopt the average of these two methods: $\log L_A/L_\odot = 3.8 \pm 0.1$ and $R_A = 47 \pm 7$ $R_\odot$.

Hipparcos observations provide the trigonometric parallax, $\pi = 1.50 \pm 0.64$ mas ($d = 667 \pm 280$ pc) for HR 4049. This, if reddening is neglected, corresponds to $\log L_A/L_\odot = 3.38 \pm 0.36$, which is in good agreement with our estimate from the photospheric parameters.
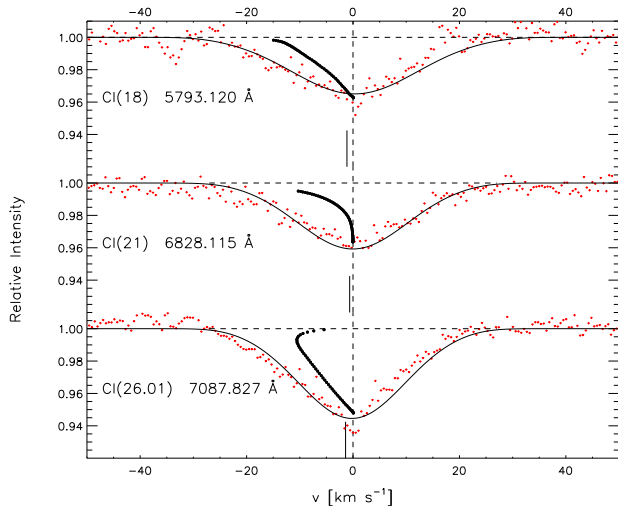
3.2. C I line profiles

Fig. 1. Line profiles of three photospheric lines ($\phi_{\rm abs} = 7.71$ at $R \approx 120,000$ with $SNR = 220$). Zero velocity has been set at the core of the profile. The velocity as derived from a Gaussian fit has been marked with a short vertical line. Typically, a Gaussian fit gives an offset from the core of the absorption lines profile of 1 km s^{-1} to the blue. For each line a synthetic line profile (thin line), and the bisectors have been computed. The velocity scale of the bisector is magnified by a factor four.

The shape of the bisector shows that there is a line asymmetry (Fig. 1, see also Paper I). Within the errors of our measurements no line profile variations are observed.

The asymmetry causes an ambiguity in the determination of the radial velocity. A Gaussian fit, or a direct integration of the line profile will give a velocity slightly blue-shifted from the core of the profile. In this work we have primarily fitted the line profiles to Gaussian functions. This introduces an estimated systematic error of 2.5 km s^{-1} in the velocities, which is significantly smaller than the variations observed in the radial velocities. Therefore, we conclude that the asymmetry does not affect the solution for the orbital parameters, with the possible exception of the systemic velocity of the system.

The shape of the bisector of HR 4049 is consistent with those of luminous F-type supergiants (Gray & Toner

1986). The velocity span of the bisector is somewhat larger for HR 4049 than for those of normal supergiants, which is likely the result of its higher luminosity. Gray & Toner (1986) suggest a two-stream granulation model to explain the line asymmetries of normal supergiants: a gas stream of cold material falls into the stars, one of hot material rises from the star. The velocity of the bisector of HR 4049 is as high as 4 km s^{-1} (Fig. 1) and suggests that HR 4049 is covered with tight-looped prominences. For such a case one would expect the outer atmosphere to show violent velocity fields resulting in chromospheric or coronal activity.

For each line displayed in Fig. 1 we have computed synthetic spectra using the line analysis program MOOG (Sneden 1973), a Kurucz model atmosphere (Kurucz 1993) for the photospheric parameters of Table 1.

3.3. Orbital parameters

In order to facilitate the discussion on HR 4049 we define the following parameters:

Primary velocity ($P_{\rm vel}$): the observed radial velocity of the primary (HR 4049 A). We used isolated absorption lines of C I, N I, and O I to determine the photospheric velocity. For most dates we have only a single order spectrum of Hα and we used the neighboring C I line at $\lambda_{\rm lab} = 6587.610$ Å to determine the photospheric velocity.

Secondary velocity ($S_{\rm vel}$): the predicted (but unobserved) radial velocity of the secondary (HR 4049 B). This velocity does, of course, depend on the mass ratio (q) of the system. Whenever needed we will assume $q = 1$, and $\sin i = 1$.

The radial velocity of the primary has been determined by measuring the velocity of photospheric absorption lines (mainly C I) on sixty nights (Table 4), spanning nine years (7.7 orbital cycles). The orbital parameters ($P_{\rm vel}$ in Tables 1 and 2) have been computed using the computer program VCURVE (Bertiau & Grobben 1969). Previous determinations of the orbital parameters by Waelkens et al. (1991a) and van Winckel et al. (1995) made use of a subset of our data and agree very well with our solution. No second period is needed to explain the radial velocity variations. In August, HR 4049 is closest to the sun and cannot easily be observed. This results in a weak alias of a year in our dataset.

In defining the orbit we follow Batten et al. (1989). Since HR 4049 has an eccentric orbit the epoch of periastron passage is defined at $\phi_{\rm rel} \equiv 0.00$ and apastron phase at $\phi_{\rm rel} \equiv 0.50$ (Fig. 2). A distinction is made between absolute and relative orbital phase. The absolute orbital phase is measured from the Julian date of the periastron passage just before the first observation in our dataset (T_0 in Table 2). The relative orbital phase is the absolute orbital phase minus the integer number of orbits since T_0. In our dataset the absolute orbital phase ($\phi_{\rm abs}$) ranges

Table 1. Stellar, orbital, and photometric parameters for HR 4049 (all parameters are measured, unless stated otherwise).

	HR 4049	Unit	Remark
	(HD 89353; SAO 17864; IRAS 10158-2844; AG Ant)		
Stellar parameters HR 4049 A (the observed component of the binary system):			
$T_{\mathrm{eff,A}}$	7500 ± 500	K	
$\log g_A$	1.0 ± 0.5	cm s^{-2}	
ζ_A	5.0	km s^{-1}	micro-turbulence
M_A	$0.56 - 0.06 + 2.50$	M$_\odot$	estimate, see text for details
$\log L_A/L_\odot$	3.8 ± 0.1		
R_A	47 ± 7	R$_\odot$	estimate, derived from L_A and $T_{\mathrm{eff,A}}$
Stellar parameters of HR 4049 B:			
$T_{\mathrm{eff,B}}$	3500	K	estimate, based on M_B, M0V (guess)
$\log g_B$	4.6	cm s^{-2}	estimate, based on M_B
M_B	0.56	M$_\odot$	estimate, based for $q = 1$, Main Sequence star
$\log L_B/L_\odot$	0.06		estimate, based on M_B
R_B	0.6	R$_\odot$	estimate, derived from L_B and $T_{\mathrm{eff,B}}$
Orbital parameters derived from HR 4049 A (the unseen component of the binary system):			
P	430.66 ± 0.28	days	orbital period
γ_{s}	-32.07 ± 0.13	km s^{-1}	systemic velocity
K_A	15.96 ± 0.19	km s^{-1}	velocity amplitude primary
e	0.30 ± 0.01		eccentricity
$T_{0,A}$	2446746.6 ± 2.4	days	epoch of periastron passage ($\phi_{\mathrm{abs}} \equiv \phi_{\mathrm{rel}} \equiv 0.0$)
ω_A	237.2 ± 2.3	degrees	longitude of periastron
$a \sin(i)$	0.60 ± 0.01	AU	semi-major axis primary
$f(M_A)$	0.158 ± 0.004	M$_\odot$	mass-function primary
$v_{\mathrm{asc}}\ (\phi_{\mathrm{asc}})$	$+13.36\ (0.25)$	km s^{-1}	velocity relative to γ_{s} (phase) of ascending node
$v_{\mathrm{des}}\ (\phi_{\mathrm{des}})$	$-18.55\ (0.91)$	km s^{-1}	velocity relative to γ_{s} (phase) of descending node
$2a(1-\epsilon)\sin(i)$	0.84	AU	estimate, periastron distance if $q = 1$
$2a(1+\epsilon)\sin(i)$	1.55	AU	estimate, apastron distance if $q = 1$
ϕ_{inf}	0.048		phase at inferior conjunction
ϕ_{sup}	0.655		phase at superior conjunction
Photometric parameters:			
V	5.52	mag.	Geneva V-band
$2 \times \Delta V$	0.24	mag.	peak-to-peak V-band
$2 \times \Delta V_1$	0.33	mag.	peak-to-peak V_1-band
$2 \times \Delta 5890$	0.30	mag.	peak-to-peak at Na I D (scaled from V_1)
$2 \times \Delta 6563$	0.27	mag.	peak-to-peak at Hα (scaled from V_1)
$HJD(m_V^{min})(\phi_{\mathrm{rel}})$	$2447235 \pm 3(0.13 \pm 0.01)$		date (phase) of photometric minimum

from 0.00 to about 8.00, while the relative orbital phase is always in the range between 0.00 and 1.00.

3.4. Photometric parameters

Waelkens et al. (1991a) have convincingly showed that the amplitude of the photometric variation increases in the blue. Since we are primarily concerned with Hα we have interpolated their amplitude versus wavelength relation to find a photometric semi-amplitude of 0.135 mag. at Hα (Table 1). For a detailed discussion of the photometric variability we refer to Waelkens et al. (1991a).

3.5. Binary properties

Table 1 gives an overview of the stellar, orbital, and photometric parameters while Fig. 3 is a scale model of HR 4049. The primary of HR 4049 is a 7500 K supergiant with a radius of $R_A = 47$ R$_\odot$. The secondary is either a M-dwarf or a WD. Since there is no UV excess and no energetic processes are observed, the M-dwarf companion is more likely. A 0.56 M$_\odot$ main sequence star (M0V) has a temperature of 3500 K and a radius of $R_B = 0.6$ R$_\odot$ ($\log L_B/L_\odot = 0.06$). The orbit of the primary has a semi-major axis of only 0.60 AU, which is 2.8 times R_A. The closest separation between the two stars (periastron passage) is 4.0 R_A and the largest separation (apastron passage) is 7.4 R_A. The binary system is surrounded by a CBD. An estimate of the distance of the inner radius of the CBD comes from the $FWHM$ of the [O I] line (Paper I), the temperature of the infrared excess (Lamers et al. 1986), and SPH simulations of CBDs (Artymowicz & Lubow 1996). All three methods give roughly the same number for the inner radius of the CBD from the center
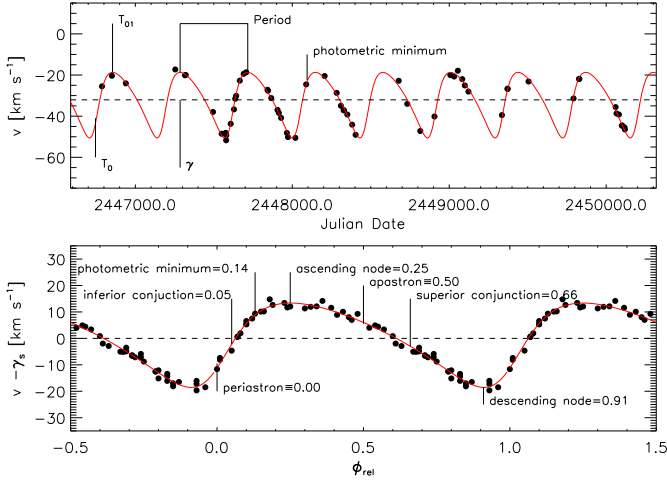
Fig. 2. Radial velocity from photospheric C I, N I, and O I lines versus Julian date and, relative to the systemic velocity, versus relative orbital phase.
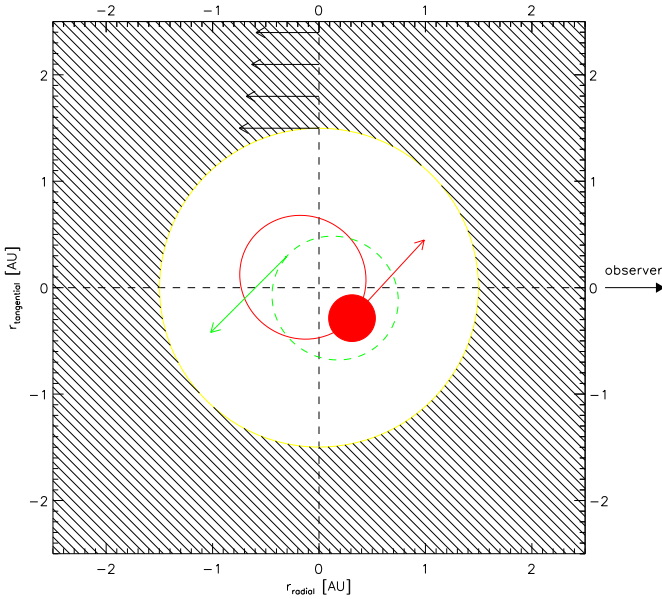
of mass (CM) of about 10 to 15 R_A, which is fairly close to twice the space occupied by the orbits of the stars.

In this paper we address the possibility of the presence of a circumprimary (CPD) and a circumsecondary (CSD) disc. These discs could possibly contribute to Hα and Na D emission or absorption. The CPD must be small in order not to reach the inner Lagrangian point which is at only $2\,R_A$ from the primary during periastron. The CSD has about the same outer radius of the CPD, but since the secondary is a small object, the inner radius is much smaller and the CSD can be more massive.

4. Na I D line profile

4.1. The marker points of the Na I D line profile

Figure 4 shows a typical Na I D_2 line profile with our definition of the marker points (see also Fig. 7 of Paper I). The extrema of the Na I D profile are labeled from blue to red as A_1, A_2, A_3, B, C_1, C_2, D, E_1, E_2, E_3 (Paper I). The broad absorption feature (which we later identify as photospheric) is labeled P and the broad emission feature is labeled A_3.
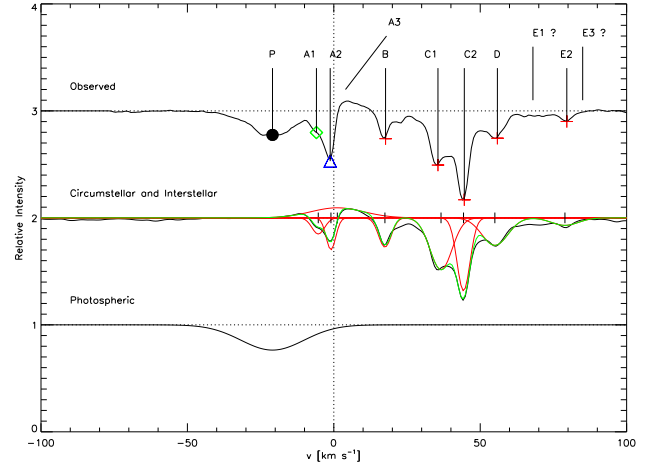

Fig. 3. A scale model for HR 4049 at periastron passage ($\phi_{\rm rel} = 0.0$). The center of mass ($r_{\rm radial}, r_{\rm tangential}$)=(0,0) is fixed and the observer is fixed at (∞,0). The solid line is the orbit of the primary, and the dashed line the orbit of the secondary. The presumed size of the secondary is not more than a period on this scale. Arrows represent velocity vectors (on a relative scale).

Fig. 4. A typical Na I D_2 line profile ($\phi_{\rm abs} = 1.93$ at $R = 60,000$) shows the main features discussed in the text. For Na I D we define eleven markers. From blue to red: P (solid dot, photosphere), A_1 and A_2 (diamond and triangle) circumsystem components, and B, C_1, C_2, D, and E_2 (plus) interstellar components. The emission (A_3) and absorption E_1 and E_3 are not measured for each individual spectrum. Using all available Na I D_2 profiles we have separated the circumstellar and interstellar components from the photospheric component. The thin lines are the Gaussian fits to the individual components and the thick line is the isolated spectrum extracted from the observations. Note that the observed spectrum is one single observations, the extracted circumstellar and interstellar, and photospheric spectra are compiled using all available Na I D_2 spectra.
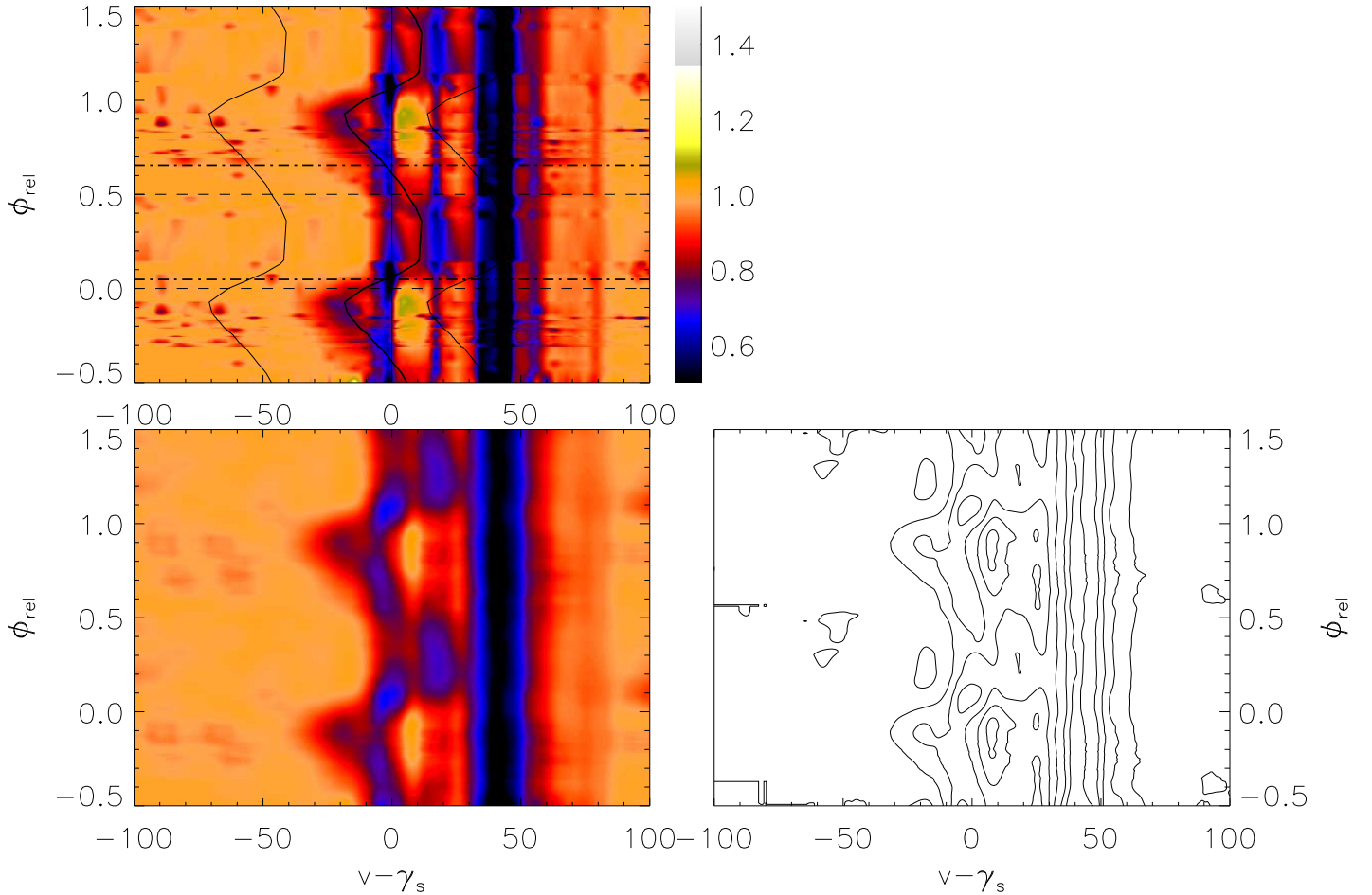
Fig. 5. Color plot of the NaI D_2 line of HR 4049. Velocity are relative to the systemic velocity. The phase covers two orbits and each spectrum is plotted twice. The thick curve represent the velocity of the primary, and the thin curves are the velocity of the primary displaced by -52.5 and +32.2 km s^{-1} (see Table 2). Periastron and apastron ($\phi_{\rm rel} = 0.0$ and 0.5 respectively) are marked with a dashed line, and inferior and superior conjunction ($\phi_{\rm rel} = 0.048$ and 0.655) with a dashed-dotted line. The left upper panel shows the spectra as observed. The lower left panel is the same data, but smoothed and filtered. The lower right panel is a contour plot of the data (10 contour lines equally space between 0.0 and 1.5).

4.2. Quantitative description of the Na I D line profiles

For the following analysis we have selected the Na I D_2 line because it is least affected by telluric water vapor lines. Figures 4 and 5 show that the line profile has several interstellar and circumsystem components which are stationary, and a photospheric component which varies in velocity. Figure 6 shows the relative velocities of the photospheric and circumstellar markers versus relative orbital phase (the interstellar markers are stationary and are not shown).

The profile of the non-photospheric contribution (plus the continuum of the star) at a given wavelength is observed if the photospheric absorption component is at a different velocity such that it does not contribute line absorption at that wavelength. Since the photospheric absorption spectrum always takes away photons, we assume that the maximum intensity at a given wavelength represents the non-photospheric spectrum. In this analysis we assume that the Na I D line radiation from circumstellar material does not vary with orbital phase. The photospheric component can now be derived from the observed spectrum and the non-photospheric spectrum. Averaging over all available spectra gives the final photospheric spectrum (see Table 2 for line parameters).

Based on our analysis we conclude that:

1. For those spectra in which we can measure the velocity of "P'," it is equal to the predicted velocity of the photosphere ($P_{\rm vel}$). We therefore conclude that "P" is photospheric.
2. All other features are stationary. Since everything connected with the primary, the secondary, or mass-flow

Table 2. Relative velocities of the marker points of the Na I D and Hα line profiles, and their orbital solution for a fixed period of $P = 430.66$ days. Errors are estimates based on the overall analysis

	Na I D$_1$			Na I D$_2$			
	$v - \gamma_s$[1]	W	$FWHM$	$v - \gamma_s$[1]	W	$FWHM$	Identification
	[km s^{-1}]	[mÅ]	[km s^{-1}]	[km s^{-1}]	[mÅ]	[km s^{-1}]	
P	variable	91 ± 2	26.3 ± 0.5	variable	124 ± 2	25.4 ± 0.5	photospheric
A$_1$	-4.6 ± 0.5	11 ± 2	4.8 ± 0.5	-5.3 ± 0.5	16 ± 2	5.1 ± 0.5	mass-loss from system
A$_2$	-0.6 ± 0.5	15 ± 2	3.6 ± 0.5	-1.0 ± 0.5	24 ± 2	3.9 ± 0.5	absorption from CBD
A$_3$	-1.0 ± 1.5	-43 ± 2	21.6 ± 0.5	1.2 ± 1.5	-42 ± 2	21.4 ± 0.5	emission from CBD
B	17.7 ± 0.5	15 ± 2	4.9 ± 0.5	17.5 ± 0.5	29 ± 2	5.1 ± 0.5	interstellar
C$_1$	36.6 ± 0.5	46 ± 2	7.8 ± 0.5	36.6 ± 0.5	90 ± 2	8.9 ± 0.5	interstellar
C$_2$	44.3 ± 0.5	59 ± 2	5.0 ± 0.5	44.3 ± 0.5	74 ± 2	5.3 ± 0.5	interstellar
D	55.0 ± 0.5	32 ± 2	10.8 ± 0.5	55.0 ± 0.5	56 ± 2	0.4 ± 0.5	interstellar
E$_1$							possibly present
E$_2$	80.4 ± 0.5	21 ± 2	15.5 ± 0.5	78.9 ± 0.5	15 ± 2	10.8 ± 0.5	interstellar
E$_3$							not confirmed

	Hα						
	$\gamma - \gamma_s$[1]	K	e	$T_0 - 2440000$	ω	rms[2]	Identification
	[km s^{-1}]	[km s^{-1}]		[HJD]	[°]		
B$_{max}$	-52.5 ± 0.6	10.0 ± 0.7	0.11 ± 0.07	6689.38 ± 47.87	224.3 ± 41.8	2.63	
B$_{min}$	-39.2[3]	16.0	0.30	6746.56	57.20	not a fit	secondary or CSD
C$_{max}$	-21.3 ± 3.5	stationary					CBD
R$_{min}$	-7.5 ± 1.6	stationary					CBD
P$_{vel}$	0.0 ± 0.1	16.0 ± 0.2	0.30 ± 0.01	6746.56 ± 02.35	237.2 ± 02.3	0.86	primary
R$_{max}$	32.2 ± 0.2	8.8 ± 0.3	0.22 ± 0.03	6707.28 ± 10.17	195.7 ± 09.2	1.57	

[1] All velocities are relative to $\gamma_s = -32.07 \pm 0.13$ km s^{-1}

[2] rms error of orbital fit to the observations, in km s^{-1}

[3] not a fit, instead assumed $q = 1$ and $\sin i = 1$, and shifted by -39.2 km s^{-1} to fit the observations

within the system must show radial velocity variations with orbital phase, we conclude that the stationary features are interstellar or circumsystem. A$_1$ is identified as mass-loss from the system with a velocity of 5.3 ± 0.5 km s^{-1}. If the Na I is not ionized at larger distance, then this velocity would represent the terminal velocity of the wind. A$_2$ is identified as absorption by the circumbinary disc. Features B, C$_1$, C$_2$, D, and E$_2$ are interstellar. E$_1$ is possibly present, and E$_3$ could not be confirmed.

3. We note the presence of a broad emission feature redward from the systemic velocity (A$_3$) which seems to be stationary. This emission feature is attributed to the CBD.

4. The separation of the Na I D$_2$ profile into a photospheric and multiple circumsystem and interstellar components leaves no room for a component associated with cool gas within the binary system: such gas must exhibit velocity variations with the orbital period.

5. The equivalent width of the photospheric Na I D$_2$ absorption must be constant. The apparent equivalent width changes due to blending by other components as it shifts in velocity.

6. Although expected, our data does not show that the equivalent widths of the circumstellar absorption components are correlated with the amount of circumstellar reddening.

4.3. The Na I D abundance

An abundance analysis for the Na I D lines has been made using the equivalent widths of the photospheric components ("P") (Table 2), $\log gf$ values after (Wiese et al. 1969), a Kurucz model atmosphere (Kurucz 1993 for the photospheric parameters of Table 1), and the line analysis program MOOG (Sneden 1973). We find that Na is depleted with an abundance of [Na/H]$=-1.6 \pm 0.2$. This depletion fits the idea of abundance versus condensation temperature: the Na abundance is considerably less depleted than Fe.

5. Hα line profile

5.1. The marker points of the Hα line profile

The marker points of Hα are the local extrema of the profile (Fig. 7).

Red maximum (R$_{max}$): a strong emission peak *always, irrespective of orbital phase*, is red-shifted from the stellar and systemic velocity.

Blue maximum (B$_{max}$): an emission peak which is blue-shifted from the stellar and systemic velocity.
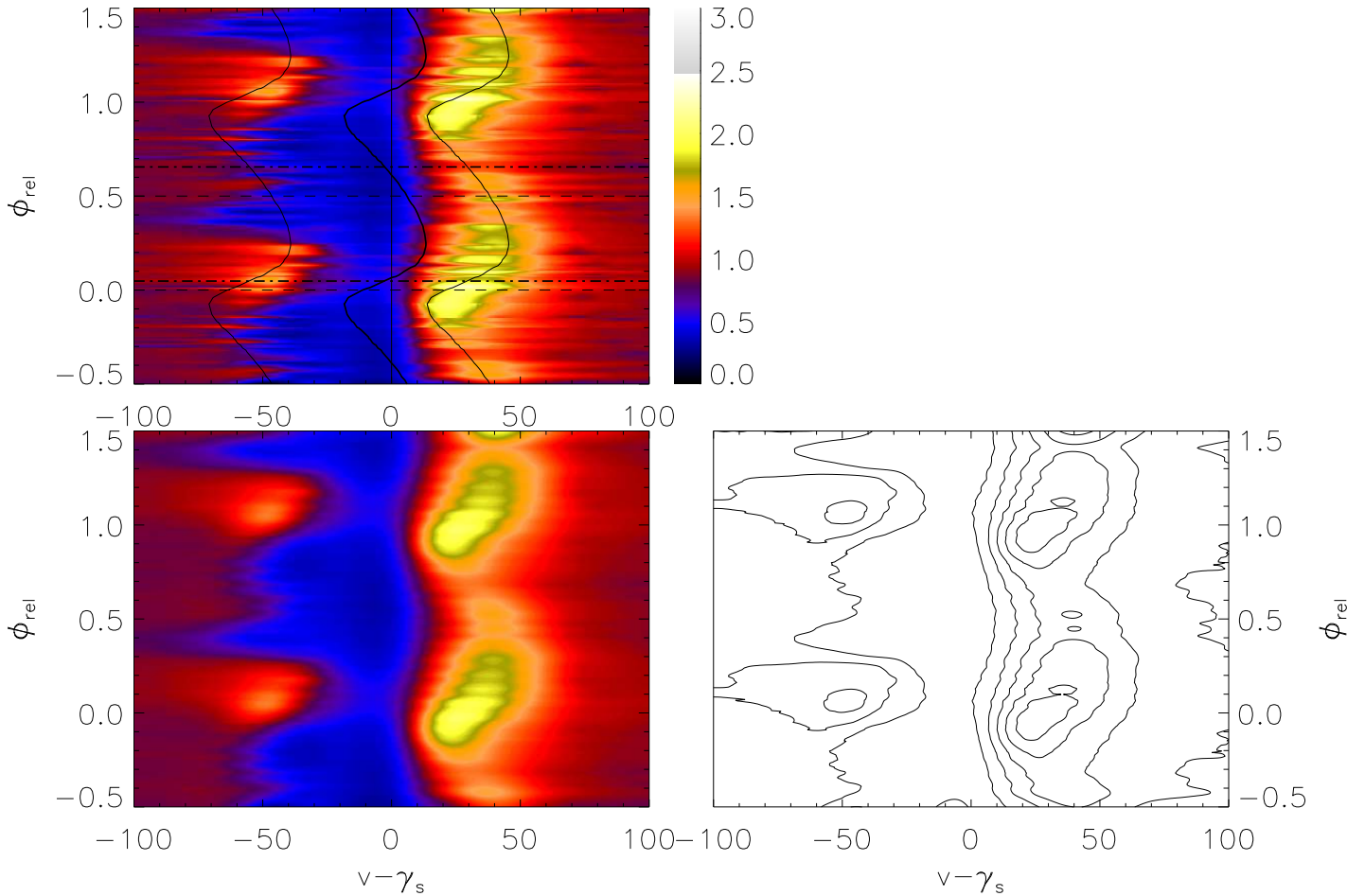
Fig. 8. Color plot of the Hα line of HR 4049. Velocity are relative to the systemic velocity. The phase covers two orbits and each spectrum is plotted twice. The thick curve represent the velocity of the primary, and the thin curves is the velocity of the primary displaced by -52.5 and +32.2 km s^{-1} (see Table 2). Note that the thin curves do not have the most appropriate velocity amplitude for B_{max} and R_{max}. Periastron and apastron ($\phi_{rel} = 0.0$ and 0.5 respectively) are marked with a dashed line, and inferior and superior conjunction ($\phi_{rel} = 0.048$ and 0.655) with a dashed-dotted line. The left upper panel shows the spectra as observed. The lower left panel is the same data, but smoothed and filtered. The lower right panel is a contour plot of the data (10 contour lines equally space between 0.0 and 3.0).

This feature is not always present and *always* weaker than R_{max}.

Red minimum (R_{min}): the most prominent minimum, and closest to R_{max}.

Blue minimum (B_{min}): a somewhat less well defined minimum, which seems only to be present for $\phi_{rel} = [0.3 - 0.9]$.

Central maximum (C_{max}): sandwiched between two minima is this local maximum.

5.2. Quantitative description of the Hα line profiles

A presentation of the Hα variability is given in Fig. 8. Velocities and relative intensities of the markers points are plotted versus relative orbital phase in Fig. 9. From an analysis of these two plots we conclude that

1. Hα emission is a function of orbital phase (Waelkens et al. 1991a). The scatter in the velocities is within the errors of our analysis. The scatter in the relative intensities is larger than expected. No clear relation is observed with time or any other parameter. We suggest that the relative intensity is governed by two processes. One which is periodic with the orbital period and responsible for the majority of the intensity variations. A second erratic process is responsible for small amplitude intensity variations.

2. A "standard" photospheric Hα absorption profile is only observed as extended wings (Fig. 7). The average equivalent width of Hα emission (from -150 to
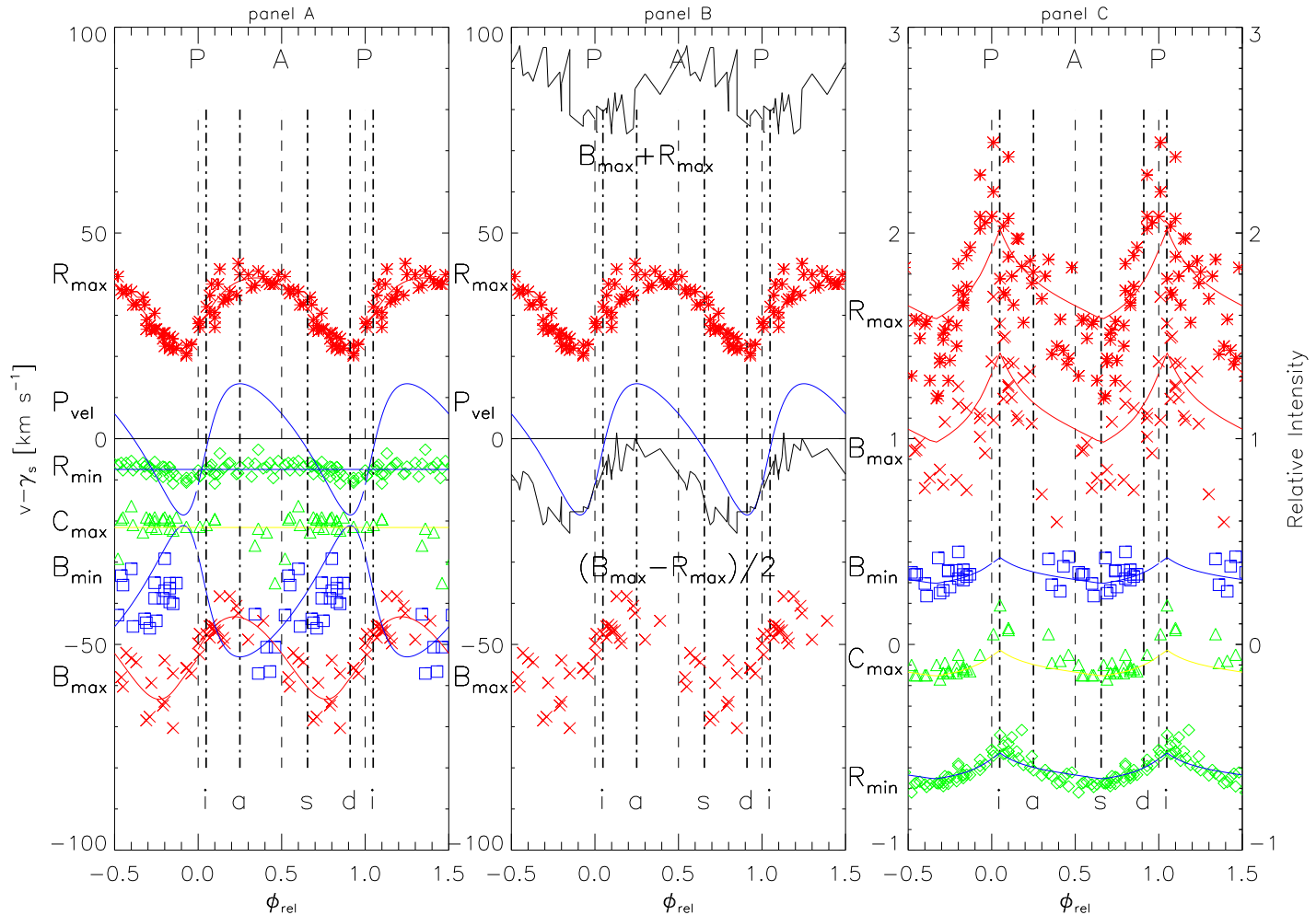
Fig. 9. The velocities (left and middle panels) and relative intensities (right panel) of the marker points of the Hα line profile. The relative intensities of C_{max} and R_{min} are shifted be -0.5 and -1.0 respectively. The dashed lines and dot-dashed lines mark periastron ("P"), apastron ("A"), inferior ("i") and superior conjunction ("s"), ascending ("a") and descending node ("d"). Note that the phase axis covers two orbits (each point is plotted twice). The middle plot shows the velocity of B_{max} and R_{max}. The thin lines in the left and middle panels are fits to the data assuming they follow a binary orbit (Table 2). The thin line in the middle panel just below zero gives the average velocity of the two markers, while the thin line near 90 km s^{-1} gives the difference between the velocity of the two marker points. The thin lines in the right panel are fits to the data for the selective reddening model (see text for details).

150 km s^{-1}) is -528 mÅ, Hα absorption (from -150 to 150 km s^{-1}) is +1133 mÅ, and for the total Hα profile (from -150 to 150 km s^{-1}) is +605 mÅ . All three equivalent widths are periodic with the orbital period (Fig. 10).

3. The velocity of R_{min} is stationary at -7.5 ± 1.6 km s^{-1}, blue-shifted from the systemic velocity. Since there is very likely a systematic shift in the velocity of R_{min} due to the presence of R_{max}, it seems most likely that the true absorption profile of R_{min} is at the systemic velocity. Some evidence that this shift is real comes from the A_1 component in the Na I D profile.

4. C_{max} has a constant velocity and must therefore be attributed to circumsystem material.

5. The velocity of R_{max} is periodic with the orbital period. We have parameterized the velocity variations by fitting an eccentric binary orbit with the orbital period (Table 1) to the radial velocities of R_{max} (Table 2). We find a velocity offset from γ_s of $+32.2\pm0.2$ km s^{-1} and a velocity amplitude a factor 0.55 times that of the primary. It seems that R_{max} leads P_{vel} by a small, possibly insignificant fraction (0.1 in phase, Table 2).

6. The velocity of B_{max} is periodic with the orbital period. The velocity offset from γ_s is -52.5 ± 0.6 km s^{-1} and the velocity amplitude is a factor 0.63 times that of the primary. B_{max} leads P_{vel} by 0.13 in phase.
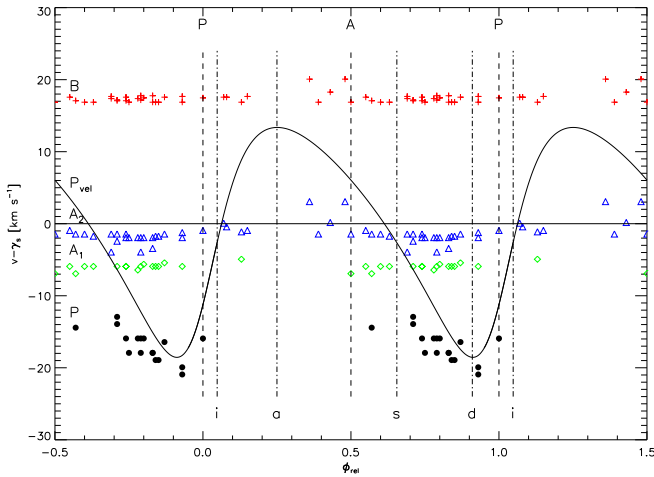
Fig. 6. The velocities of the photospheric and circumsystem markers of the Na I D_2 line profile. The dashed lines and dot-dashed lines mark periastron ("P"), apastron ("A"), inferior ("i") and superior ("s") conjunction, ascending ("a"), and descending node ("d"). The phase axis covers two orbits (each point is plotted twice).
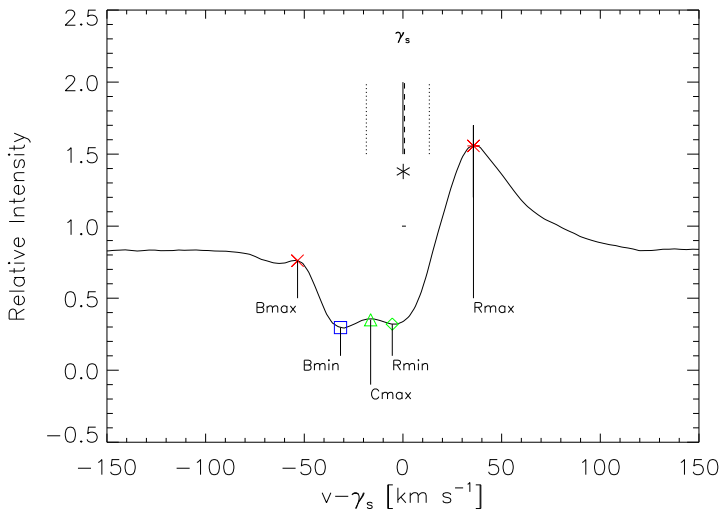

Fig. 7. A typical Hα line profile ($\phi_{abs} = 2.60$ at $R = 60,000$) showing the main characteristic features discussed in the text. For Hα we define seven markers. From blue to red: blue maximum (cross), blue minimum (open square), central maximum (open triangle), red minimum (open diamond), red maximum (asterisk), and the fixed relative intensity markers (plus). The solid vertical line marks the systemic velocity (γ_s) with on both sides a short-dashed line at the extreme velocity of the star in its orbit. The long-dashed line is the stellar velocity (P_{vel}) at the date when this spectrum was obtained.
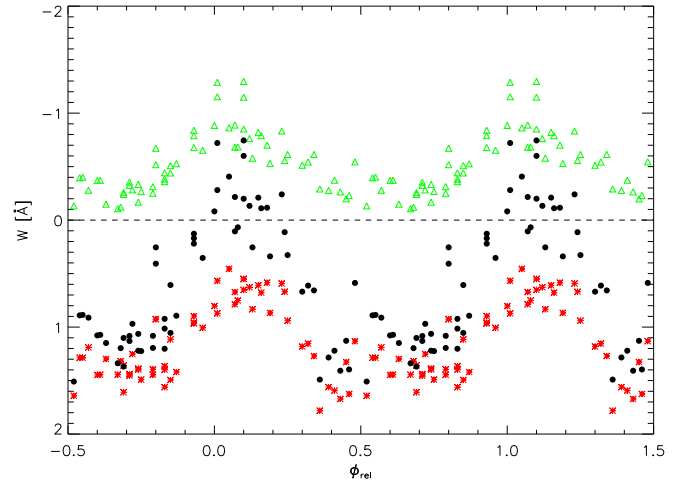

Fig. 10. Hα emission (triangles), absorption (asterisk), and total (solid dots) equivalent width versus relative orbital phase. Equivalent width of emission lines are negative and those for absorption lines positive.

7. The average velocity of R_{max} and B_{max}, $(R_{max}+B_{max})/2$., is not constant relative to P_{vel} or to the systemic velocity (middle panel of Fig. 9). Near $\phi_{rel} = 0.0$ the average velocity is P_{vel}. Maximum displacement from P_{vel} of -18 km s^{-1} occurs at $\phi_{rel} = [0.2 - 0.7]$. The velocity difference between R_{max} and B_{max}, $(R_{max}-B_{max})$, reaches a maximum near superior conjunction of 96 km s^{-1} and a minimum near inferior conjunction of 74 km s^{-1} with an average difference of 85 km s^{-1}.

8. The velocity of B_{min} is clearly variable, but the phase coverage is far from continuous. It seems that the radial velocity variations are in anti-phase with the primary (P_{vel}). Maybe this marker traces wind material from the secondary in the line-of-sight to the primary, or an accretion disc around the secondary.

9. The average velocity of R_{max} and B_{max} is close to B_{min} (see middle panel of Fig. 9). This could indicate that both R_{max} and B_{max} are from a single emission feature with a central absorption.

10. The relative intensity of all marker points is a function of the relative orbital phase. Maximum relative intensity is reached near $\phi_{rel} \sim 0.07 \pm 0.1$ (periastron and inferior conjunction) while minimum relative intensity is reached near $\phi_{rel} \sim 0.61 \pm 0.1$ (superior conjunction). In the phase diagram, it rises steeply to maximum relative intensity and decreases slowly to minimum relative intensity. Since the phase difference from inferior to superior conjunction is $\Delta\phi_{rel} = 0.54$ ($\Delta\theta = 180°$), and from superior to inferior conjunction only $\Delta\phi_{rel} = 0.46$ ($\Delta\theta = 180°$), this asymmetric behavior suggests that the relative intensity is a function of θ (the position angle from periastron) and that the relative intensities are the same for the receding and approaching part

of the orbit. R_{min} best demonstrates that maximum relative intensity is reached at inferior and minimum relative intensity at superior conjunction.

11. The intensity ratio between maximum and minimum relative intensity of R_{max} (corrected for the continuum of) is $(2.1-1)/(1.4-1)=2.8$. If the Hα emission does not participate in the reddening, we would expect an intensity ratio of 1.6. These are about the same numbers and suggest that we should investigate a model in which the Hα intensity variations are due to different amounts of reddening towards the star and the Hα emitting region.

5.2.1. Discussion on velocities of C_{max} and R_{min} and the circumbinary disc

Interestingly, C_{max} and R_{min} are stationary. The source of C_{max} and R_{min} must therefore lie outside the binary orbit. Possible sources are the circumbinary disc and mass-loss from the system. We will argue that the circumbinary disc gives the best explanation for the observations.

For a rotating circumbinary disc we would expect a double peaked emission profile superimposed on a photospheric spectrum. In this case C_{max} can be identified as due to approaching material. The peak due to receding material is hidden in the emission from the much stronger R_{max}. The phase-dependent circumsystem reddening suggests that we are dealing with a thick, relative hot circumbinary disc. In that case we have absorption (here identified as R_{min}) from the circumbinary disc of the photospheric spectrum. We therefore suggest that the profile between -21.3 and -7.5 (from C_{max} to R_{min}) is from the circumbinary disc. Assuming that the total mass of the binary system is 1.2 M$_{\odot}$ (see Table 1) we find that C_{max} is at a distance of 2.4 AU ($=10.7\ R_A$) from the center of mass for an edge-on disc, and the orbital period of CBD material is 1200 days (see Fig. 3 for a scale model of the binary system).

Mass-loss from the system by means of an expanding circumbinary disc is not a valid option for the presence of R_{min}. An expansion velocity of 7.5 km s^{-1} would lead to an expansion of 1.8 AU ($=8.4\ R_A$) of the disc per orbital period. There are no indications that the system loses its circumbinary disc at such a high rate, nor that it replenishes its disc at this rate. Therefore an expanding circumbinary disc is not a valid option to explain the presence of R_{min}.

Since we have argued that the line forming region must be outside the binary system, it must be at least 3.5 R_A from the star. Hα emission from stellar winds is confined to several stellar radii from the star and can therefore not account for C_{max} and R_{min}.

In conclusion we suggest that C_{max} is emission from the approaching part of the CBD and that the emission from the receding part of the CBD is lost in the much

stronger R_{max} feature. R_{min} is due to absorption by the CBD.

5.2.2. Discussion on the velocities of B_{max} and R_{max}

The shape and strength of the B_{max} and R_{max} are a function of relative orbital phase and the source of the emission should therefore be sought within in the binary nature of the system. The fact that the radial velocities of B_{max} and R_{max} vary in similar ways, suggests that B_{max} and R_{max} are related. Since B_{max} and R_{max} do not have the same velocity offset from P_{vel} this suggests that B_{max} and R_{max} may be one and the same emission feature separated by an absorption feature. We will refer to this feature as the double peaked emission (DPE). This absorption feature is centered around R_{min}. An important clue about the location of their line forming region is given by the velocity amplitude of B_{max} and R_{max}. The velocity amplitude of B_{max} and R_{max} are about the same, and only half the velocity amplitude of the primary.

In conclusion we argue that B_{max} and R_{max} are part of a strong emission feature with an absorption around 7.5 km s^{-1} blue-shifted from the center.

5.2.3. Discussion on intensities and selective reddening

The intensity of R_{min} suggests that there is a correlation between its relative intensity and orbital phase such that maximum relative intensity is reached near inferior conjunction and minimum near superior conjunction. Although the exact phases of maximum and minimum relative intensity are less well defined for the other marker points, the data suggest a similar dependence on orbital phase. This indicates that the relative intensities of the marker points are not related to the distance between the stars (which would give a maximum at periastron passage and a minimum at apastron passage). Instead it suggests that the projected location of the stars in their orbit causes the variability.

We have investigated the possibility that the continuum and the line emission have constant absolute intensities, but experience different amounts of circumsystem reddening. The resulting fits are over plotted in the right panel of Fig. 9 c and show that this model can account for the shape and amount of the relative intensity variations.

If the Hα emission originates from the secondary or CSD, the line emission and the continuum experience different amounts of circumsystem reddening and the photometric amplitude at Hα (Table 1) can account for the observed relative intensity variations. If the line emission originates from the CBD the reddening at Hα must be twice as high as derived from the photometry. The reason for this is that the Hα emission has a constant absolute flux and reddening effects only the stellar continuum. If the line emission originates from close to the primary, the model predicts no variations in Hα line emission.

The fact that we need a somewhat higher reddening for the CBD model is not a severe problem since the exact reddening towards different region of the system is not known and the Hα emission might be stronger near periastron than apastron (this is however a second order effect). This model can also account for the erratic small amplitude relative intensity variations of B_{max} and R_{max} as due to inhomogeneities in the line of sight to the Hα emitting region, which causes small variations in reddening.

In conclusion we argue that the relative intensity variations of the marker points are the result of a different amounts of circumsystem reddening towards the star and Hα line emission. A second order periodic variation is possibly present for which Hα emission is stronger near periastron than apastron passage.

6. Model for Hα emission and variability

The velocities of the markers B_{max}, B_{min}, and R_{max} vary with the orbital period (Fig. 9). In the simplest possible model, a P-Cygni profile results from the primaries spherically symmetric wind. The relative intensity of R_{max} and B_{min} are phase independent, and their velocities follow the orbital motion of the primary. The observed velocities vary indeed with the orbital period but the velocity amplitude of R_{max} and B_{max} are only 60 % that of the primary. B_{min} could be moving in anti-phase with the primary, and the relative intensity of R_{max}, B_{max}, C_{max}, and R_{min} vary strongly with orbital phase, reaching a pronounced maximum near inferior conjunction. This simple geometry of a stellar wind can thus not account for the smaller velocity amplitude and the larger relative intensities near inferior conjuction.

Following our analysis of the Hα marker points we propose two competing models.

Model I: starlight reflects on the circumbinary disk: material orbiting the center of mass at a larger distance than the primary, will have a lower velocity amplitude (if in Keplerian motion). In this model the velocity amplitudes of B_{max} and R_{max} indicate that the line forming region is at about 12 AU (55 R_A) from the CM. There is a circumbinary disc at a distance of about ten stellar radii, but this material has an orbital period which is larger than that of the primary (about 1200 days). In this model light from the primary reflects on a small part of the circumbinary disc (a spot) which is closest to the primary. The spot propagates through the disc with the angular speed of the primary. In this case we see the radial velocity of the spot (the Keplerian velocity of the circumbinary disc) and a velocity amplitude expected for the CBD, but the period will be that of the primary. Since the spot is supposedly always near the inner radius of the CBD which is closest to the primary, it will experience a roughly constant reddening as the spot propagates through the disc: the absolute intensity of the Hα line emission will be constant with orbital phase (to first order). The stellar continuum

on the other hand, experiences a phase-dependent reddening. The contrast between the Hα emission and the stellar continuum, which is measured as the relative intensity of Hα, varies with orbital phase: maximum relative intensity near inferior conjunction, and minimum relative intensity near superior conjunction. This is consistent with the observations. In order to reflect line radiation (Hα) and not stellar continuum photons, the temperature of the inner region of the CBD where the reflection occurs must be high enough to have $n = 1$ of the Hydrogen atom populated, dust to be absent, and Na to be ionized (since we do not see the same variability in Na I D). Additional there could be a second order variability such that Hα emission is stronger near periastron than apastron.

This model suggests that B_{max} and R_{max} are formed in the CBD, and are indeed one and the same emission profile with a central absorption. The $FWHM$ of the emission profile is about 120 km s^{-1}, while the central absorption has a $FWHM$ of about 50 km s^{-1}. It seems that the $FWHM$ of the emission feature is not significantly smaller during inferior and superior conjunction (when all Keplerian velocities have a projected velocity of zero) than at ascending and descending node (when we see the maximum and minimum velocity). This favors a model in which a random velocity field (turbulence) is the source of line broadening and not the Keplerian motion within the disk.

Model II: activity in the extended atmosphere (chromosphere, corona, or wind): In this model, we propose that the major contribution to the Hα emission comes from the extended atmosphere of the primary. The velocity of the central absorption (R_{min}, or the average velocity of B_{max} and R_{max}) is a measure for the velocity of the line forming region. This suggests an outflow velocity which ranges from 0 to 18 km s^{-1}. The outflow velocity (< 18 km s^{-1}) is of the same order as the velocity of the star in its orbit (16 km s^{-1}), but much less than the escape velocity of the primary (70 km s^{-1}). This means that if material leaves the surface of the star it will fall back unless the acceleration continous while Hα is ionized. In this model, the intensity variations can still be attributed to different amounts of reddening towards the star and the Hα emitting volume, if the latter is formed at a large enough distance from the star. This means that the emission comes from several stellar radii. Since material at such a large distance from the star will experience the gravitation pull from the secondary, it follows a different orbit than the primary. this could explain why the two emission peaks move with a velocity amplitude about half that of the primary.

Artymowicz & Lubow (1996) have simulated binary systems with a circumbinary disc and find that material falls through a gap towards the stars. The material in this flow is accreted onto the star(s), either by direct impact from a stream, or via an accretion disc. Such an accre-

tion mechisme could be responsible for the activities in the extended atmosphere and the Hα variability.

In order to further develop this model, we need first to understand chromospheric activities of normal post-AGB stars, followed by a study to see how these activities can be locked to the orbital motion of the primary. Some support for this model can be found in the line asymmetry of C I lines which we have attributed to granulation and could be related to the activity of the extended atmosphere of HR 4049.

7. Discussion

The Hα and Na I D line profiles of HR 4049 are clearly varying with the orbital period. The C I line profiles are asymmetric but show no variations with orbital phase. The asymmetry is likely due to granulation. The changes in the observed line profiles of Na I D are due to the Doppler shift of the photospheric component relative to the circumstellar and interstellar emission and absorption spectrum. There are several interstellar absorption components (B, C_1, C_2, and E_2), a broad absorption from the circumbinary disc (A_2), and emission from the approaching part of the CBD (A_3), and a weak mass-loss component (A_1) at a velocity of only 5.3 ± 0.5 km s^{-1}.

For Hα we identify photospheric component, only detectable as extended absorption wings (Fig. 11). The CBD absorbs (R_{min}) and emits (C_{max}) in Hα. The absorption from the CBD is 7 km s^{-1} blue-shifted from the systemic velocity. If this shift is real, it could suggest that we see a photospheric spectrum reflected by circumstellar material. In such a scenario the systemic velocity derived from the photospheric spectrum represent the velocity component in the direction of the mirror and not towards the observer. Furthermore, the mirror could have a small velocity. The critical question here is what is the systemic velocity from CO radio observations. Unfortunately no such data is available.

There is a weak emission feature at -21.3 ± 3.5 km s^{-1} relative to the systemic velocity, which originates from the circumbinary disc. The two strong shell type Hα emission peaks are from one single broad emission feature with a central absorption feature centered around -7.5 km s^{-1} relative to the center of the emission. The intensity variations are best explained as due to a differential amount of reddening towards the Hα emitting region and the stellar continuum, with a possible second order variation such that Hα emission is stronger near periastron than apastron. The radial velocities suggest that the Hα emission moves in phase with the primary, but with a slightly lower velocity amplitude.

We proposed two competing models. In both models the Hα profile is interpreted as a single broad emission feature with a central absorption, and the relative intensity variations are attributed to a different amount of reddening toward the Hα emitting volume and the stellar contin-

uum. In model I, Hα emission is from reflected starlight on a localized spot in the circumbinary disc. In model II, the Hα emission originated from the extended atmosphere of the primary.

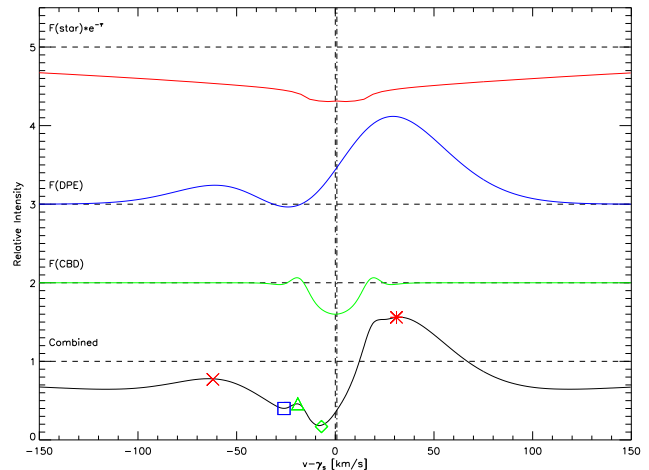**Fig. 11.** Composite of the Hα profile. From top to bottom (with increasing distance from the star): The photospheric profile of the primary, the double peaked emission (DPE), emission and absorption from the CBD, and the composite profile. This combined profile depends on the phase since the photospheric spectrum is experiencing a phase-dependent reddening.

There is considerable similarity between the HR 4049's Hα profile and that of SU Aur, an early-type T Tauri star (ETTS, Herbst et al. 1994, other members are CO Ori, RY Tau, and RY Lup) with an accretion disc viewed almost edge on - see Hα profiles published by Giampapa et al. (1993), Johns & Basri (1995), and Fig. 3 of Petrov et al. (1996). In both stars, the red emission is more pronounced than the blue emission with a central absorption near the systemic velocity. It is this similarity that drew our attention to the models proposed to account for the Hα and other Balmer line profiles. Although the Hα profiles of HR 4049 and SU Tau are similar in form, they are different in scale: the emission for SU Tau is spread over a velocity range that is about eight times that seen here for HR 4049. This difference is likely traceable to the higher surface gravity of SU Tau and the related differences in escape velocity ($v \approx 70$ km s^{-1} for HR 4049 but $v \approx 511$ km s^{-1} for SU Tau) or in Keplerian velocity at a fixed distance from the star. Giampapa et al. (1993) proposed a two component wind model for SU Aur: an optically thin wind moving at high velocity outside a slow, optically thick wind. Johns & Basri (1995) proposed an alternative model with a slow moving (or stationary) region close to the star with a very high turbulence velocity, and a wind at a terminal velocity of about 50 km s^{-1}. In this model, the wind originates in the disc at the place where the disc's Keplerian angular velocity is equal to

the star's angular rotation rate (typically at a distance of 3 R_A). The central absorption in SU Aur is from the stellar wind which leaves the disc at 150 km s^{-1} and decelerate due to the gravitational force of the stars and absorbs at a terminal velocity of 50 km s^{-1}. Interestingly, the photometry varies non-periodically and it has been suggested that this is due to variable circumstellar extinction. From a Fourier analysis of line profiles, Bouvier et al. (1986) claim that SU Aur is a double lined spectroscopic binary, but the binary nature of SU Aur has not been confirmed using speckle imaging (Ghez et al. 1993). Based on presence of a disc and the similar shape of the Hα emission, it is tempting to believe that the emitting region of SU Aur might resemble that of HR 4049.

It is interesting to speculate in which respect our proposed models for Hα emission could help to understand the gas-dust separation process. First of all, it seems that all metal-depleted post-AGB binaries have Hα emission (from very weak (BD +39°4926) to extremely strong (HR 4049 and HD 44179)) that is periodic with the orbital period (this is confirmed for HR 4049 and HD 213985) It is not evident that the Hα emission is related to the metal-depleted nature of the star. BD +39°4926 which is extremely metal depleted has very little Hα emission, but also post-AGB stars which are not in a binary system show Hα emission which is variable (HD 56126 and HD 133656). Therefore we argue that the variability of the Hα emission cannot be linked directly to the metal-depleted nature of the post-AGB stars. Instead it seems that the Hα emission and the metal-depleted photosphere are both the result of the binary nature of these stars and the geometry of their circumstellar environment.

Based on our analysis we suggest to proceed with a detailed study on the shape of the bisector with orbital phase. This could lead to a better understanding of the effect of granulation in post-AGB stars. Spectropolarimetric observations of Hα and other emission lines could distinguish between reflected and direct light. Finally, the selective reddening scenario can be tested with simultaneous high-resolution spectroscopy and photometry.

References

Artymowicz P., Lubow S.H., 1996, ApJ 467, L77

Bakker E.J., van der Wolf F.L.A., Lamers H.J.G.L.M. et al., 1996, A&A 306, 924 (Paper I)

Batten A.H., Fletcher J.M., MacCarthy D.G., 1989, Publications of the Dominion Astrophysical Observatory 17, 1

Bergeron P., Saffer R.A., Liebert J., 1992, ApJ 394, 228

Bertiau F.C., Grobben J., 1969, Ric. Astron. Specola Vaticana 8, 1

Boothroyd A.I., Sackmann, I.J., 1988, ApJ 328, 641

Bouvier J., Bertout C., Benz W., Mayor M., 1986, A&A 165, 110

Buss Jr. R.H., Cohen M., Tielens A.G.G.M. et al., 1990, ApJ 365, L23

Ghez A.M., Neugebauer G., Matthews K., 1993, AJ 106, 2005

Giampapa M.S., Basri G.S., Johns C.M., Imhoff C.L., 1993, ApJS 89, 321

Giridhar S., Rao N.K., Lambert D.L., 1994, ApJ 437, 476

Gonzalez G., Wallerstein G., 1996, MNRAS 280, 515

Gonzalez G., Lambert D.L., Giridhar S., 1997a, ApJ 479, 427

Gonzalez G., Lambert D.L., Giridhar S., 1997b, ApJ 481, 452

Gray D.F., Toner C.G., 1986, PASP 98, 499

Herbst W., Herbst D.K., Grossman E.J., Weinstein D., 1994, AJ 108, 1906

Johns C.M., Basri G., 1995, ApJ 449, 341

Joshi U.C., Deshpande M.R., Sen A.K., Kulshrestha A., 1987, A&A 181, 31

Kurucz R. L., 1993, ATLAS9 Stellar Atmosphere Programs and 2 km s^{-1} Grid CDROM Vol. 13 (Cambridge: Smithsonian Astrophysical Observatory)

Lambert D.L., Hinkle K.H., Luck R.E., 1988, ApJ 333, 917

Lamers H.J.G.L.M., Waters L.B.F.M., Garmany C.D., Perez M.R., Waelkens C., 1986, A&A 154, L20

Mathis J.S., Lamers H.J.G.L.M., 1992, A&A 259, L39

McCarthy J.K, Sandiford B.A., Boyd D., Booth J., 1993, PASP 105, 881

Molster F.J., van den Ancker M.E., Tielens A.G.G.M. et al., 1996, A&A 315, L373

Petrov P.P., Gullbring E., Ilyin I. et al., 1996, A&A 314, 821

Sneden C., 1973, Ph.D. thesis, University of Texas

Tull R.G., MacQueen P.J., Sneden C., Lambert D.L., 1995, PASP 107, 251

Unger S., 1994, La Palma Technical Notes No. XXIII

van Winckel H., Mathis J.S., Waelkens C., 1992, Nat 356, 500

van Winckel H., Waelkens C., Waters L.B.F.M., 1995, A&A 293, L25

Venn K.A., Lambert D.L., 1990, ApJ 363, 234

Waelkens C., Lamers H.J.G.L.M., Waters L.B.F.M., Rufner F., Trams N.R., Le Bertre T., Ferlet R., Vidal-Madjar A., 1991a, A&A 242, 433

Waelkens C., van Winckel H., Bogaert E., Trams N.R., 1991b, A&A 251, 495

Waters L.B.F.M., Trams N.R., Waelkens C., 1992, A&A 262, L37

Wiese W.L., Smith M.W., Miles B.M., 1969 "Atomic Transition Probabilities: Volume II Sodium Through Calcium", NSRDS-NBS 22

Appendix (only available in electronic form)

Table 3. Log of 32 Na I D observations.

Date		HJD	ϕ_{abs}	Tel./Instr.	$R = \lambda/\Delta\lambda$	v_{rad}^1 [km s^{-1}]
Nov	29 1988	2447495.021	1.74	McD/CS11	60000	-40.46
Dec	17 1988	2447513.031	1.78	McD/CS11	60000	-43.56
Jan	23 1989	2447549.938	1.87	McD/CS11	60000	-49.31
Feb	02 1989	2447575.613	1.93	CAT/CES	55000	-50.45
Feb	22 1989	2447579.868	1.93	McD/CS11	60000	-50.14
Mar	23 1989	2447608.752	2.00	McD/CS11	60000	-42.96
Apr	21 1989	2447637.634	2.07	McD/CS11	60000	-31.05
Apr	26 1989	2447642.673	2.08	McD/CS11	60000	-29.20
May	19 1989	2447665.628	2.13	McD/CS11	60000	-22.90
Nov	12 1989	2447842.987	2.55	McD/CS11	60000	-28.31
Dec	06 1989	2447867.018	2.60	McD/CS11	60000	-31.42
Jan	11 1990	2447902.890	2.69	McD/CS11	60000	-36.71
Jan	24 1990	2447915.670	2.71	CAT/CES	55000	-38.78
Feb	06 1990	2447928.861	2.75	McD/CS11	60000	-41.00
Mar	02 1990	2447952.798	2.80	McD/CS11	60000	-45.13
Mar	15 1990	2447965.769	2.83	McD/CS11	60000	-47.25
Mar	22 1990	2447972.816	2.85	McD/CS11	60000	-48.30
Nov	11 1990	2448207.002	3.39	McD/CS11	60000	-21.50
Dec	30 1990	2448255.962	3.50	McD/CS11	60000	-26.23
Jan	26 1991	2448282.914	3.57	McD/CS11	60000	-29.47
Feb	22 1991	2448309.859	3.63	McD/CS11	60000	-33.13
May	03 1991	2448379.610	3.79	McD/CS11	60000	-44.47
May	22 1991	2448398.625	3.84	McD/CS11	60000	-47.59
Feb	25 1992	2448678.000	4.48	WHT/UES	50000	-25.29
Mar	08 1993	2449055.000	5.36	WHT/UES	50000	-20.51
Apr	05 1993	2449083.000	5.43	WHT/UES	50000	-22.75
Apr	19 1995	2449826.634	7.15	McD/CE	45000	-21.53
Dec	08 1995	2450059.996	7.69	McD/CE	45000	-37.32
Dec	14 1995	2450065.987	7.71	McD/CS21	120000	-38.29
Dec	29 1995	2450080.924	7.74	McD/CS21	145000	-40.79
Jan	19 1996	2450101.896	7.79	McD/CE	60000	-44.41
Feb	03 1996	2450116.838	7.83	McD/CE	45000	-46.90

[1] Heliocentric radial velocities are computed using the orbital parameters

Table 4. Log of 60 Hα observations.

Date		HJD	ϕ_{abs}	Tel./Instr.	$R = \lambda/\Delta\lambda$	$v_{\mathrm{rad}}^{2,3}$
Dec	23 1986	2446787.771	0.10	CAT/CES	55000	-26
Feb	24 1987	2446850.708	0.24	CAT/CES	55000	-20
May	24 1987	2446939.583	0.45	CAT/CES	55000	-24
Apr	07 1988	2447254.672	1.18	CAT/CES	55000	-17
Jun	04 1988	2447316.610	1.32	CAT/CES	55000	-20
Jun	09 1988	2447321.625	1.34	CAT/CES	55000	-20
Nov	29 1988	2447494.940	1.74	McD/CS11	60000	-38
Jan	23 1989	2447549.890	1.87	McD/CS11	60000	-49
Feb	18 1989	2447575.647	1.93	CAT/CES	55000	-48
Feb	21 1989	2447578.725	1.93	CAT/CES	55000	-52
Feb	22 1989	2447579.820	1.93	McD/CS11	60000	-49
Mar	22 1989	2447607.780	2.00	McD/CS11	60000	-44
Apr	12 1989	2447628.680	2.05	CAT/CES	55000	-37
Apr	20 1989	2447636.620	2.07	McD/CS11	60000	-32
Apr	26 1989	2447642.650	2.08	McD/CS11	60000	-30
May	19 1989	2447665.680	2.13	McD/CS11	60000	-23
Jun	13 1989	2447690.630	2.19	McD/CS11	60000	-19
Jun	29 1989	2447706.507	2.23	CAT/CES	55000	-19
Nov	11 1989	2447842.010	2.54	McD/CS11	60000	-27
Nov	14 1989	2447845.010	2.55	McD/CS11	60000	-28
Dec	05 1989	2447866.010	2.60	McD/CS11	60000	-31
Jan	14 1990	2447905.920	2.69	McD/CS11	60000	-37
Jan	23 1990	2447914.691	2.71	CAT/CES	55000	-38
Feb	06 1990	2447928.820	2.75	McD/CS11	60000	-41
Mar	15 1990	2447965.740	2.83	McD/CS11	60000	-48
Mar	22 1990	2447972.860	2.85	McD/CS11	60000	-50
May	08 1990	2448019.650	2.96	McD/CS11	60000	-51
Aug	02 1990	2448088.450	3.12	CTIO/ES	18000	-25
Nov	10 1990	2448206.010	3.39	McD/CS11	60000	-20
Jan	26 1991	2448282.880	3.57	McD/CS11	60000	-29
Feb	22 1991	2448309.820	3.63	McD/CS11	60000	-35
Mar	11 1991	2448326.796	3.67	McD/CS11	60000	-37
Mar	14 1991	2448329.608	3.68	CAT/CES	55000	-37
Apr	04 1991	2448350.654	3.72	McD/CS11	60000	-39
May	05 1991	2448381.589	3.80	McD/CS11	60000	-44
May	27 1991	2448403.607	3.85	McD/CS11	60000	-49
Feb	25 1992	2448678.000	4.48	WHT/UES	50000	-23
Apr	20 1992	2448732.535	4.61	CAT/CES	55000	-34
Jul	10 1992	2448815.482	4.80	CAT/CES	55000	-47
Oct	10 1992	2448905.883	5.01	CAT/CES	55000	-40
Jan	19 1993	2449006.789	5.25	CAT/CES	55000	-20
Feb	12 1993	2449030.710	5.30	CAT/CES	55000	-21
Mar	08 1993	2449055.000	5.36	WHT/UES	50000	-18
Apr	05 1993	2449083.000	5.43	WHT/UES	50000	-22
Apr	22 1993	2449099.513	5.46	CAT/CES	55000	-25
May	14 1993	2449122.460	5.52	CAT/CES	55000	-28
Dec	14 1993	2449335.782	6.01	CAT/CES	55000	-39
Jan	19 1994	2449371.710	6.10	CAT/CES	55000	-27
Jan	19 1994	2449371.744	6.10	CAT/CES	55000	-27
May	31 1994	2449505.466	6.41	CAT/CES	55000	-23
Mar	15 1995	2449791.754	7.07	McD/CE	45000	-31
Apr	19 1995	2449826.634	7.15	McD/CE	45000	-22
Apr	21 1995	2449828.637	7.16	McD/CE	45000	-22
Dec	08 1995	2450059.996	7.69	McD/CE	45000	-36
Dec	14 1995	2450065.987	7.71	McD/CS21	120000	-39
Dec	29 1995	2450080.924	7.74	McD/CS21	145000	-39
Jan	17 1996	2450099.871	7.79	McD/CE	60000	-45
Jan	19 1996	2450101.896	7.79	McD/CE	60000	-45
Feb	03 1996	2450116.838	7.83	McD/CE	45000	-45
Feb	06 1996	2450118.825	7.83	McD/CE	45000	-46

[2] Heliocentric radial velocities are measured from CI , N I, and O I lines
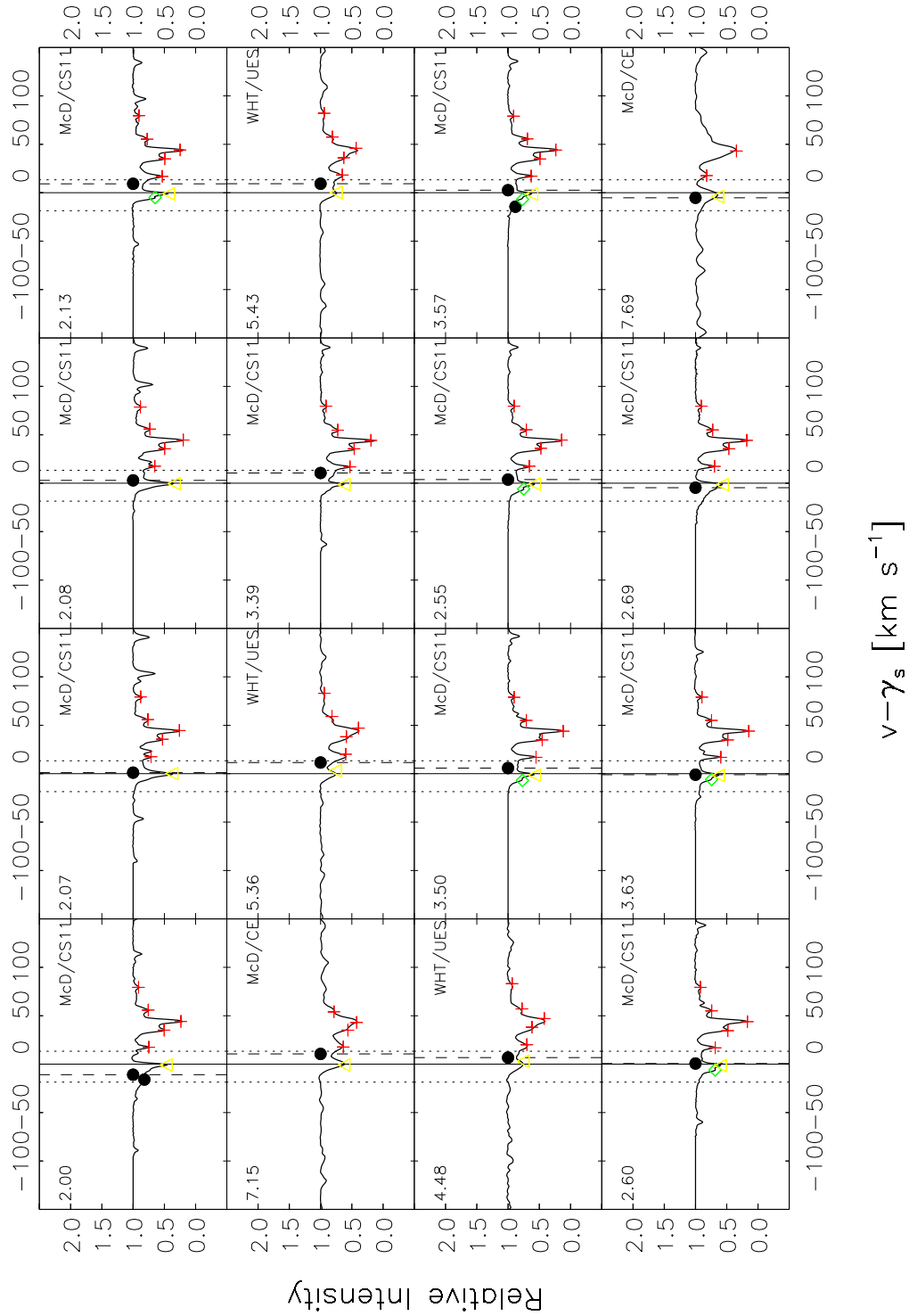[3] velocity accuracy of 2 km s^{-1}

Fig. 12. The observed Na I D$_2$ line profiles in order of relative orbital phase $\phi_{\rm rel}$. The systemic velocity of the binary, $\gamma_{\rm s} = -32.15$ km s^{-1}, is at zero (solid line) with on both sides a short-dashed line at the extreme velocity of the star in its orbit. The long-dashed lines correspond to the velocity of that star. The measured velocities and intensities of the marker points are marked. The photospheric component (on the profile, only if measured) and the predicted stellar velocity (at an intensity of 1.0) have both been plotted with a dot. These two points can be at different velocities because the photospheric velocity cannot be very well determined from the observed Na I D$_2$ profile. The circumsystem markers (diamond and triangle) and the interstellar markers (crosses) have been marked. In each window, the upper left corner gives the absolute orbital phase and the upper right corner the telescope/instrument with which the spectrum was obtained.
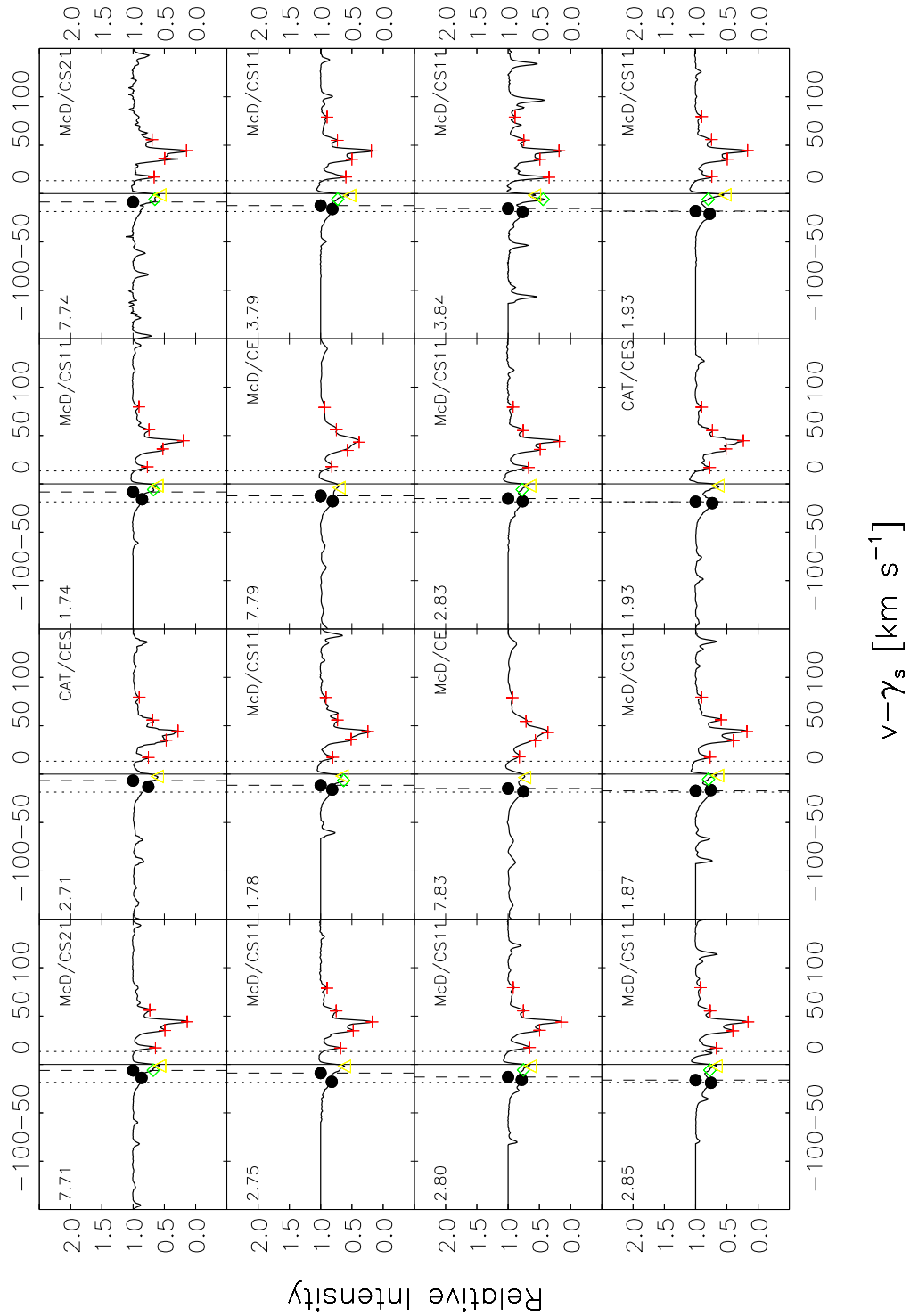
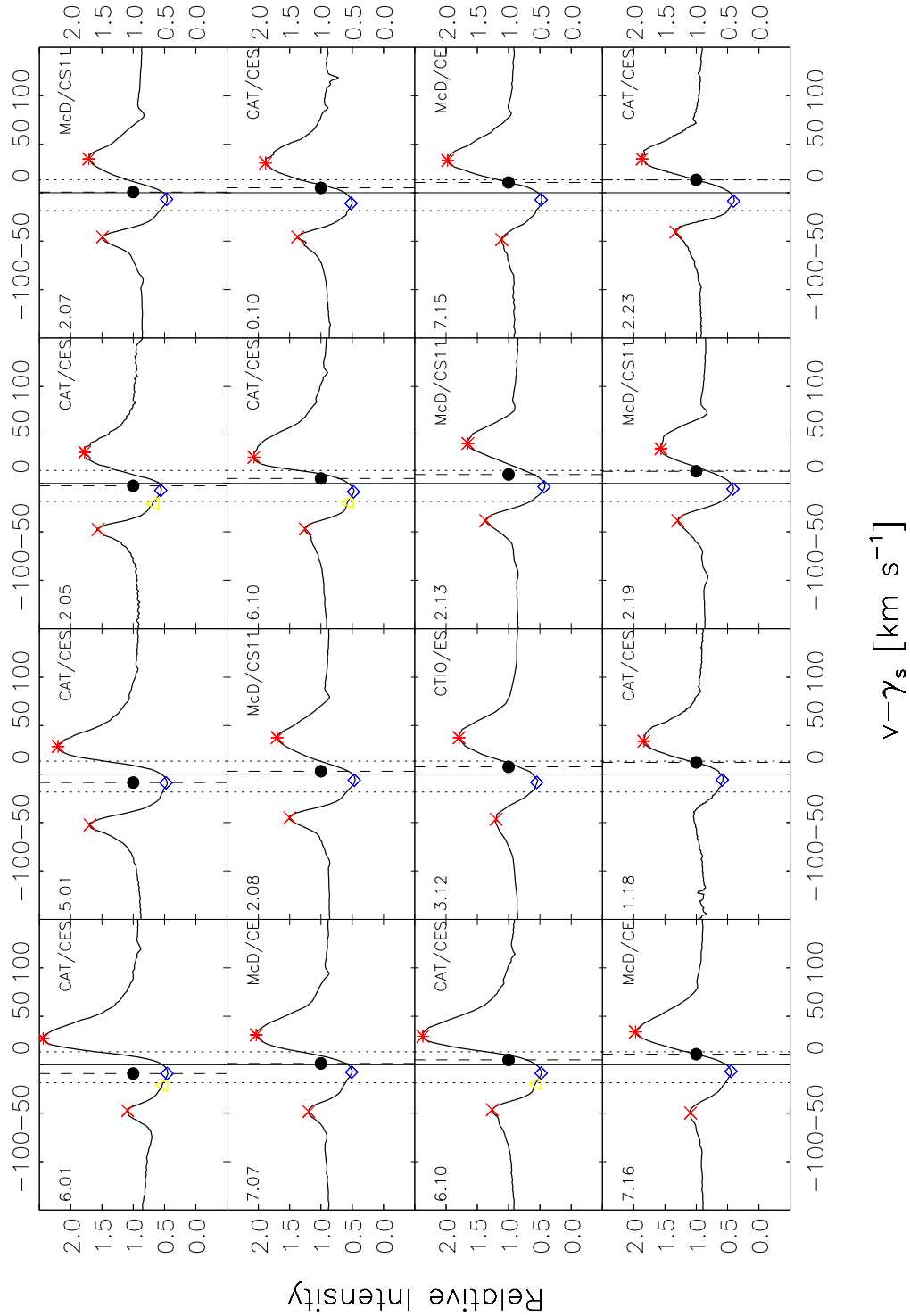**Fig. 13.** Continued: the observed Na I D$_2$ line profiles.

Fig. 14. The observed Hα line profiles in order of relative orbital phase $\phi_{\rm rel}$. The systemic velocity of the binary, $\gamma_{\rm s} = -32.15$ km s^{-1}, is at zero (solid line) with on both sides a short-dashed line at the extreme velocity of the star in its orbit. The long-dashed lines correspond to the velocity of that star. The "blue maximum" (cross), "blue minimum" (open square), "central maximum" (open triangle), "red minimum" (open diamond), and "red maximum" (asterisk) have been marked. In each window, the upper left corner gives the absolute orbital phase and the upper right corner the telescope/instrument with which the spectrum was obtained.
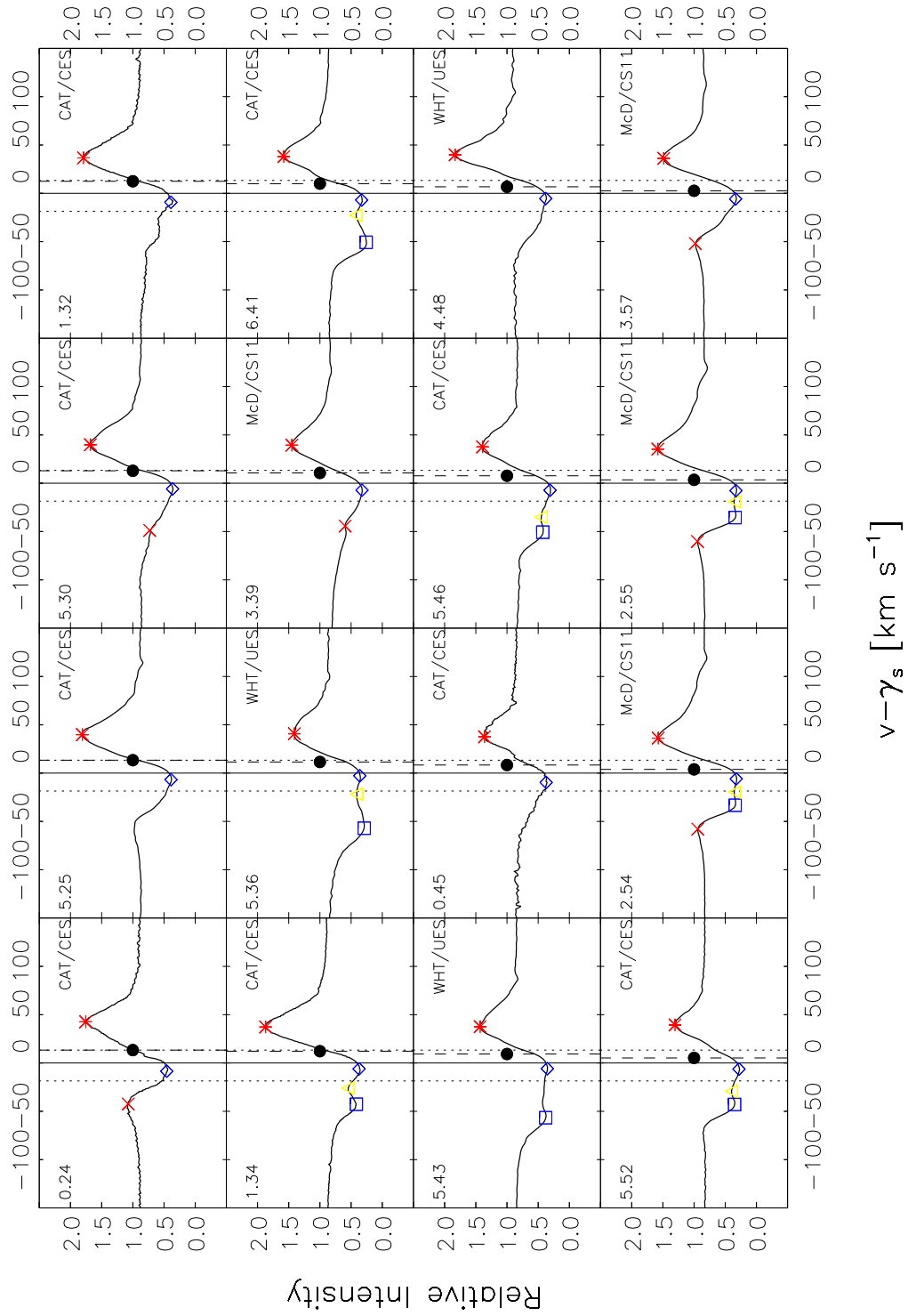
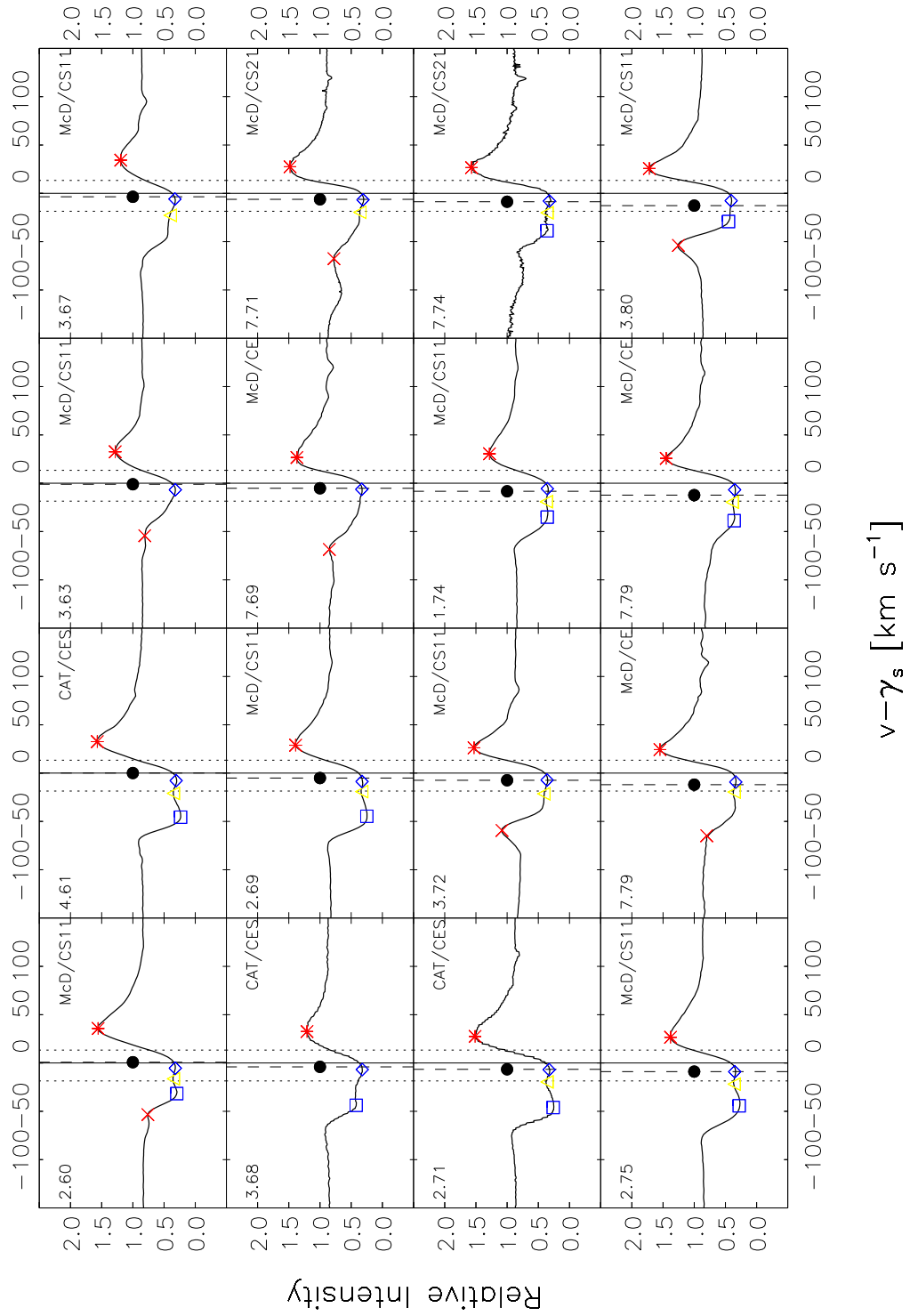**Fig. 15.** Continued: the observed Hα line profiles.

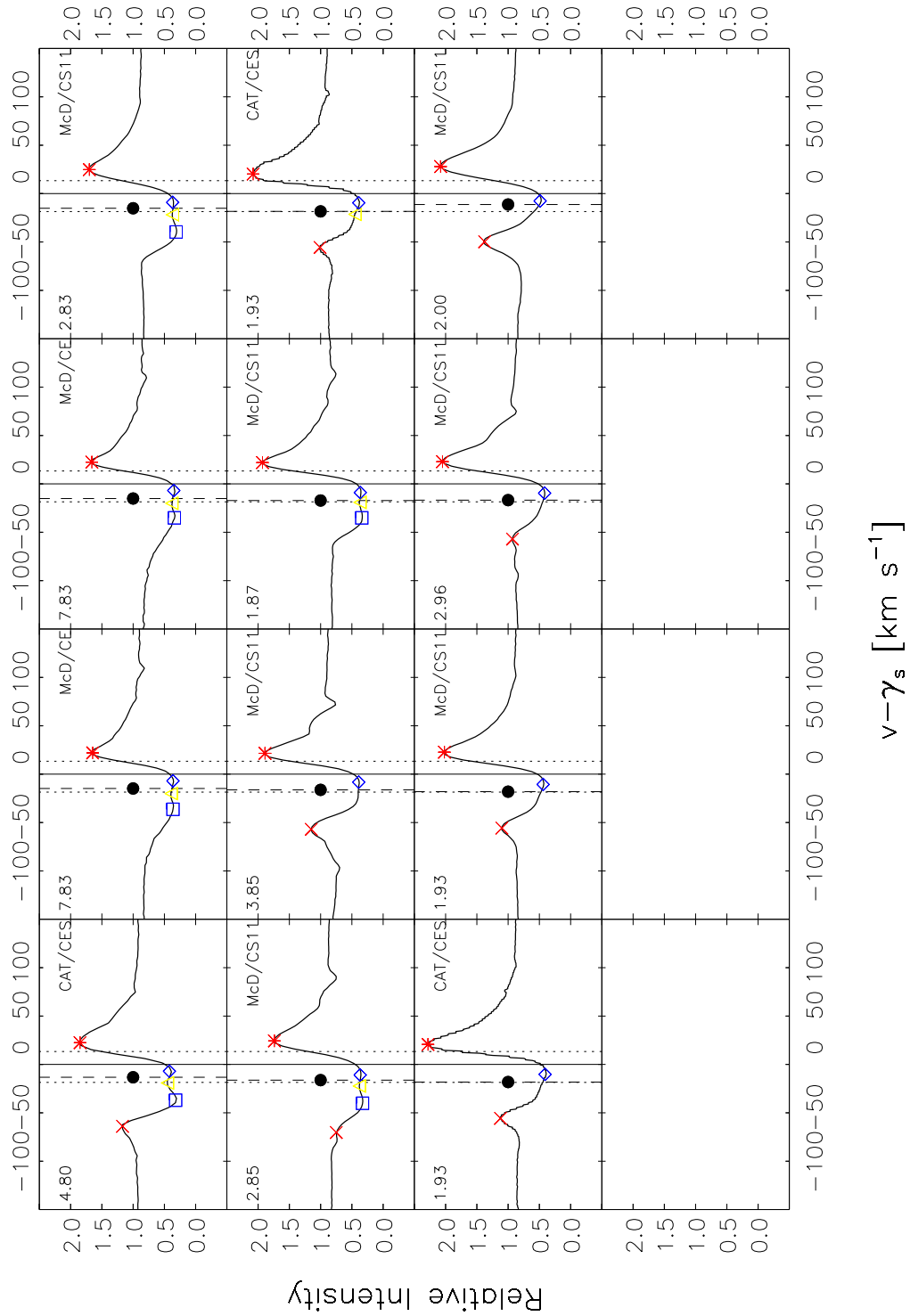**Fig. 16.** Continued: the observed Hα line profiles.

Fig. 17. Continued: the observed Hα line profiles.